

Article

# Pore-Scale Investigation of the Electrical Property and Saturation Exponent of Archie's Law in Hydrate-Bearing Sediments

Jinhuan Zhao <sup>1,2</sup>, Changling Liu <sup>1,2,\*</sup>, Chengfeng Li <sup>1,2</sup>, Yongchao Zhang <sup>1,2</sup>, Qingtao Bu <sup>1,2</sup>, Nengyou Wu <sup>1,2</sup>, Yang Liu <sup>3</sup> and Qiang Chen <sup>1,2</sup>

<sup>1</sup> Key Laboratory of Gas Hydrate, Ministry of Natural Resources, Qingdao Institute of Marine Geology, Qingdao 266237, China; zhaojinhuan99@yeah.net (J.Z.); lchengfeng@mail.cgs.gov.cn (C.L.); zhangyongchao@mail.cgs.gov.cn (Y.Z.); qingtiao-bu@edu.cn (Q.B.); wuny@ms.giec.ac.cn (N.W.); cqiang@mail.cgs.gov.cn (Q.C.)

<sup>2</sup> Laboratory for Marine Mineral Resources, Qingdao National Laboratory for Marine Science and Technology, Qingdao 266237, China

<sup>3</sup> School of Geophysics and Information Technology, China University of Geosciences, Beijing 100083, China; Lyang@cugb.edu.cn

\* Correspondence: lchangling@mail.cgs.gov.cn

**Abstract:** Characterizing the electrical property of hydrate-bearing sediments is essential for hydrate reservoir identification and saturation evaluation. As the major contributor to electrical conductivity, pore water is a key factor in characterizing the electrical properties of hydrate-bearing sediments. The objective of this study is to clarify the effect of hydrates on pore water and the relationship between pore water characteristics and the saturation exponent of Archie's law in hydrate-bearing sediments. A combination of X-ray computed tomography and resistivity measurement technology is used to derive the three-dimensional spatial structure and resistivity of hydrate-bearing sediments simultaneously, which is helpful to characterize pore water and investigate the saturation exponent of Archie's law at the micro-scale. The results show that the resistivity of hydrate-bearing sediments is controlled by changes in pore water distribution and connectivity caused by hydrate formation. With the increase of hydrate saturation, pore water connectivity decreases, but the average coordination number and tortuosity increase due to much smaller and more tortuous throats of pore water divided by hydrate particles. It is also found that the saturation exponent of Archie's law is controlled by the distribution and connectivity of pore water. As the parameters of connected pore water (e.g., porosity, water saturation) decrease, the saturation exponent decreases. At a low hydrate-saturation stage, the saturation exponent of Archie's law changes obviously due to the complicated pore structure of hydrate-bearing sediments. A new logarithmic relationship between the saturation exponent of Archie's law and the tortuosity of pore water is proposed which helps to calculate field hydrate saturation using resistivity logging data.

**Keywords:** saturation exponent; hydrate-bearing sediments; pore water; resistivity; X-ray computed tomography



**Citation:** Zhao, J.; Liu, C.; Li, C.; Zhang, Y.; Bu, Q.; Wu, N.; Liu, Y.; Chen, Q. Pore-Scale Investigation of the Electrical Property and Saturation Exponent of Archie's Law in Hydrate-Bearing Sediments. *J. Mar. Sci. Eng.* **2022**, *10*, 111. <https://doi.org/10.3390/jmse10010111>

Academic Editor: Timothy S. Collett

Received: 18 December 2021

Accepted: 11 January 2022

Published: 14 January 2022

**Publisher's Note:** MDPI stays neutral with regard to jurisdictional claims in published maps and institutional affiliations.



**Copyright:** © 2022 by the authors. Licensee MDPI, Basel, Switzerland. This article is an open access article distributed under the terms and conditions of the Creative Commons Attribution (CC BY) license (<https://creativecommons.org/licenses/by/4.0/>).

## 1. Introduction

Gas hydrates are regarded as a potential energy resource in the 21st century due to its tremendous reserves and clean combustion [1]. The industrial development of gas hydrates is of great significance in achieving carbon neutralization and researchers have paid increasing attention to their exploration and exploitation. Gas hydrates, composed of water and gas molecules, are crystalline, which structures are usually considered to be non-conductive materials [2]. The resistivity of the bulk sediment rises because of the existence of gas hydrates [3]. Therefore, characterizing the resistivity of hydrate-bearing sediments is of significance in hydrate saturation calculation.

The electrical conductivity of hydrate-bearing sediments mainly depends on ions in pore water [4]. The resistivity of hydrate-bearing sediments is strongly dependent on both pore fluid conductivity and fluid volume fraction [5–7]. Hydrates, as solid materials, change the original pore water distribution and connectivity, which causes a significant change of resistivity [8]. When hydrates exist in the throat of the pores, blocking the electrical conductive path, the resistivity of hydrate-bearing sediments will increase significantly [9]. Archie's law was proposed by Archie in 1942 to describe the relationship between the resistivity of sediments and pore water saturation in porous rocks [10]. To explain non-Archie behavior and obtain accurate water saturation information, many researchers have focused on studying the parameters of Archie's law. The results show that the parameters of Archie's law are not constant and are influenced by pore geometrical factors [11–18]. With respect to gas hydrates, the saturation exponent of Archie's law calculated from field logging data changes significantly with the sites [3,19,20]. Different empirical values for the saturation exponent are reported in different experiments [2,5,21,22]. The value of the saturation exponent is very difficult to select in hydrate-bearing sediments because of the complicated pore structure caused by various pore habits of hydrates. Cook and Waite suggested that the value of the saturation exponent should be  $2.5 \pm 0.5$  if independent estimates are not available [17]. However, studies have revealed that the saturation exponent is a function of water saturation and pore geometrical factor rather than a constant [5,23,24].

X-ray computed tomography (X-CT), as a non-destructive method, has been extensively used to investigate the micro-distribution of each component in hydrate-bearing sediments [25–29]. Based on a three-dimensional X-CT image of hydrate-bearing sediments, pore water geometrical factors (pore size distribution, tortuosity, and coordination number representing the geometry, distribution, and connectivity of pore fluid) can be obtained and the volume of each component can be calculated. Therefore, it is possible to investigate resistivity and the saturation exponent of Archie's law in hydrate-bearing sediments at the micro-scale. Dong et al. used X-CT to explore the influence of the micro-distribution of hydrates on the resistivity of hydrate-bearing sediments [23]. They thought that different conductive paths would be generated due to hydrate formation. However, the relationship between hydrates and the pore water of hydrate-bearing sediments has not yet been clarified. Zhang et al. extracted pore area and tortuosity fractal dimensions for effective pores from CT images of xenon hydrate-bearing alumina ball packings to investigate the relationship between tortuosity and saturation exponents [24]. Xenon hydrate-bearing alumina ball packings are only an analog for hydrate-bearing sediments and may not simulate closely enough the actual pore geometrical factors in hydrate-bearing sediments.

In this study, the joint measurement of X-ray computed tomography and resistivity is used to determine the micro-distribution of methane hydrates, the pore geometrical factors of pore water, and the resistivity of hydrate-bearing sediments simultaneously. The effects of hydrates on resistivity and the saturation exponent are discussed. This study aims to clarify the resistivity property of hydrate-bearing sediments and proposes a feasible method to determine saturation exponents.

## 2. Experiments and Methods

### 2.1. Experimental Device

The experimental device contains three main parts: an X-ray CT scanner, a low-temperature high-pressure vessel, and a resistivity measurement system (Figure 1). The type of X-ray CT scanner is a Phoenix v|tome|xS, GE Sensing & Inspection Technologies, with a nano-focus X-ray source and a 16-bit digital flat panel detector [30].

The low-temperature high-pressure vessel is made of PEEK material, with an inner diameter of 35.0 mm. The maximum confining pressure of the vessel is 10.0 MPa. A hollow cylindrical rubber barrel with an inner diameter of 25.0 mm and a height of 42.0 mm is arranged in the vessel, which is used to hold sediments. The high-pressure environment for hydrate formation is simulated by confining fluid outside the rubber and pore fluid

inside the rubber. A pressure transducer and a temperature probe are used for monitoring pore fluid pressure and confining fluid temperature.

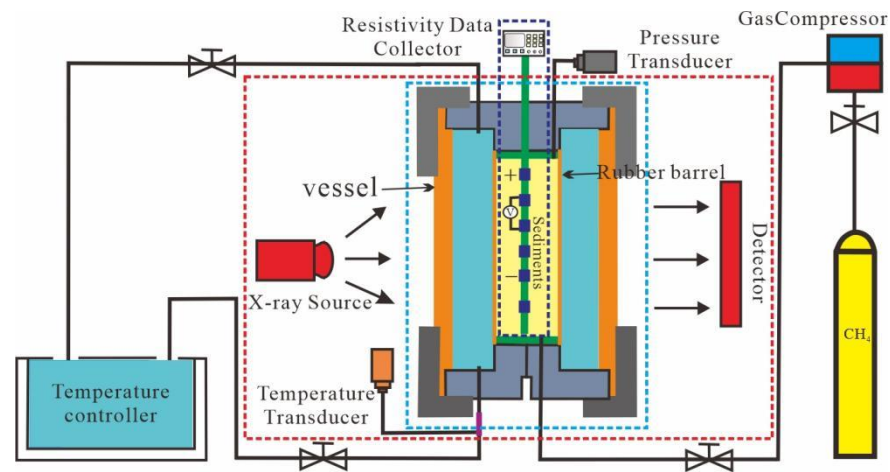


Figure 1. Schematic of experimental device.

The resistivity measurement system utilizes a six-electrode probe and quadrupole method. Six electrode rings, made of stainless steel, are equally spaced and fixed by C-bars. Four adjacent electrodes, as a group, accomplish the resistivity measurement of a layer. The resistivity of another layer is collected by changing the measurement electrodes into current injection electrodes. Therefore, the resistivity of the upper, middle, and lower layers is collected. The probe can withstand a maximum pressure up to 10.0 MPa.

### 2.2. Experimental Procedure

Quartz sands with particle sizes of >500 μm are chosen as host sediments in the hydrate-formation experiments. The pore fluid of sediments is 3.5 wt% NaCl solution. Methane hydrates are formed in the sediments with initial pore fluid saturation of 100%. Methane gas (purity > 99.99%) was injected into the sediments to reach the designed pore fluid pressure. Glycol, as a confining fluid, was injected into the space between the vessel and the rubber to provide confining pressure. Under the high-pressure condition provided by pore fluid pressure and confining pressure, the sediments containing NaCl solution and methane gas are cooled by a temperature controller to generate methane hydrates. According to the methane hydrate phase boundary [31], six tests are set to generate hydrates with different saturations. Detailed information about the experiments is provided in Table 1.

Table 1. Summary of test conditions.

Test	Initial Pressure <sup>1</sup> /MPa	Final Pressure <sup>2</sup> /MPa	Temperature <sup>3</sup> /°C	Initial Water Saturation/%	Duration <sup>4</sup> /h
1	5.18	3.17	0.2	95.04	46
2	5.54	3.45	1.0	82.34	39
3	5.54	4.18	2.8	93.01	24
4	5.54	5.23	3.5	78.42	16
5	4.99	4.32	1.5	81.73	22
6	4.99	4.42	1.4	80.60	43

<sup>1</sup> Initial pressure is the pore fluid pressure before the formation of hydrate. <sup>2</sup> Final pressure is the pore fluid pressure after the formation of hydrate, which is the moment when the temperature and pressure are stable. <sup>3</sup> Temperature is the experimental temperature in sediments which is controlled by temperature controller. <sup>4</sup> Duration is the time taken fore hydrate formation.

According to the sample size, the X-CT scan was operating at a voltage of 120 kV, a current of 100 μA, and with a detector exposure time of 1000 ms. The size of the flat panel

detector was  $1024 \times 1024$  pixels. The 3D image resolution of X-CT scanning image was  $45 \mu\text{m}$ , which means the size of each voxel was  $45 \mu\text{m} \times 45 \mu\text{m} \times 45 \mu\text{m}$ . The magnification was 4.44. The X-CT scans were conducted when the temperature and pressure were stable to avoid the blurring of the X-CT image caused by phase changes during hydrate formation. The measurement of resistivity was conducted at the same time, which can ensure the consistency between the resistivity and CT image of hydrate-bearing sediments. We collected resistivity information for only the upper and lower layers due to the circuit problem. The resistivity measurement of the three layers being independent, the data of the upper and lower layers are credible.

### 2.3. X-CT Image Analysis

Various 2D X-ray images of sediments, obtained after the X-CT scan, were analyzed with VG Studio MAX and Avizo software. The three-dimensional images of the sediments were reconstructed using the optimized Feldkamp algorithm based on 2D X-ray images. Components, including gas, water, hydrate, and sand, were discriminated by segmenting the gray histograms with a threshold value of each component. Then, the distribution characteristics of hydrate and pore fluid could be observed. Generally, the size of the representative volume element (RVE) was 8 to 10 times the particle size [32]. We chose a cube with dimensions of  $180 \times 180 \times 180 \text{ pixel}^3$  as our RVE. The size of the cube is  $8100 \mu\text{m} \times 8100 \mu\text{m} \times 8100 \mu\text{m}$  ( $180 \times 45 \mu\text{m}$ ), which is 10 times greater than the particle sizes ( $10 \times 500 \mu\text{m}$ ). The volume of each component and the pore water parameters of the RVE were calculated.

## 3. Results and Discussion

### 3.1. Analysis of Resistivity Changes with Hydrate Growth

According to the spatial distribution of the hydrate grains within the host sediment, the morphology of hydrate in sediments can be generally divided into grain-displacing or pore fluid-displacing hydrate [33]. For coarse-grained sand, used in our experiments, pore fluid-displacing hydrate was generated. Hydrates formed from dissolved methane (Figure 2a) and on a water–gas interface (Figure 2b) are both observed in X-CT images.

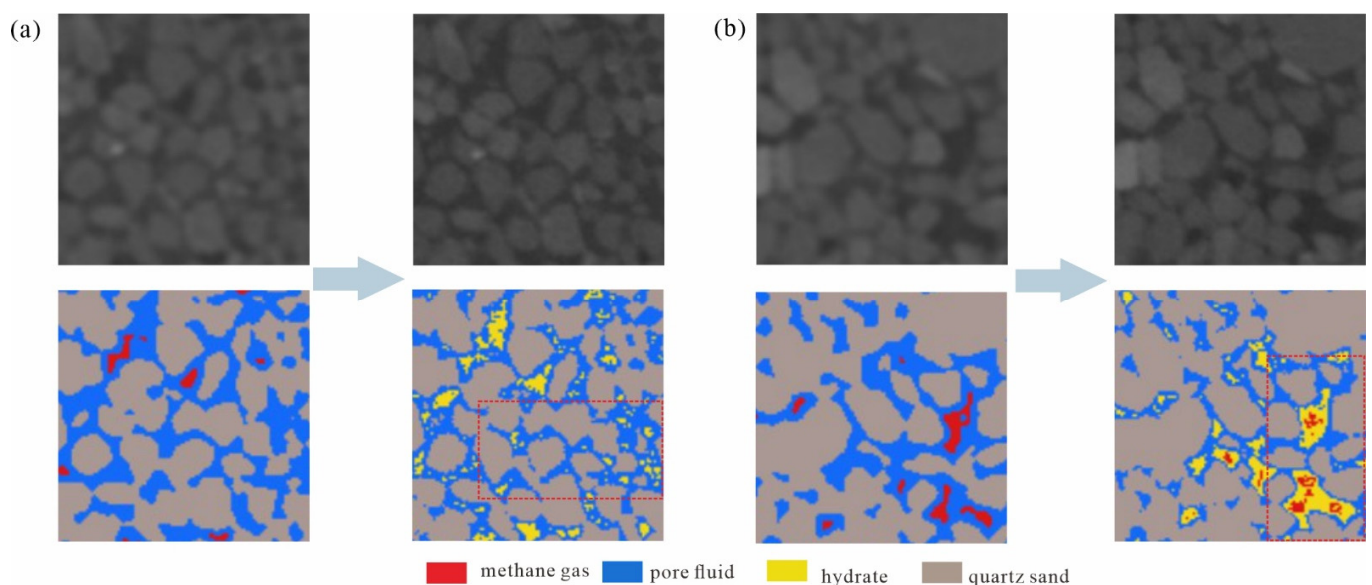


**Figure 2.** The two types of hydrate formation observed from the X-CT image. The left-hand images in (a,b) present the initial stage in which hydrate saturation is zero. The right-hand images in (a,b) present hydrate formation in pores. Hydrates formed from dissolved methane in the quadrilateral area of (a), and hydrates formed on a water–gas interface in the quadrilateral area of (b).

The resistivity of hydrate-bearing sediments with different saturations are shown in Figure 3. The resistivity varies between 1 Ω·m and 4 Ω·m, and the hydrate saturation varies between 0 and 0.5. Generally, the higher the hydrate saturation is, the bigger the resistivity. However, resistivity versus hydrate saturation presents various changes, which can be divided into three cases. The first case is a significant difference in resistivity when hydrate saturation is similar; for example, the upper and lower layers of test 3 in Figure 3. At the end of hydrate formation, the pore is almost entirely occupied by hydrates, which means the current path is blocked. Compared to the situation in which the hydrates are dispersed in pores, resistivity will obviously increase. In the second case, there is a slight difference in resistivity change when hydrate saturation undergoes a significant change. Resistivity varies from 1.16 Ω·m to 1.94 Ω·m when the hydrate saturation changes from 0 to 0.45 in test 1. We can observe that the methane gas is wholly consumed to form hydrates with water and is partially converted to hydrates. The rest remains in its initial place or changes slightly in the pores containing methane gas and water. Methane gas, like hydrate, is a non-conductive material. The contribution to the resistivity of hydrate-bearing sediments can be regarded as unchanged when methane gas is converted into hydrate. Hence, there may be no or only a slight change of resistivity. In the third case, there is a reduction degree of resistivity in test 6. The effect of “salt removal” during hydrate formation increases the salinity of pore water [8]. The resistivity of hydrate-bearing sediments will decrease if the pore water has not been trapped by hydrates. We can conclude that hydrates change resistivity by changing the distribution and connection of pore water. The conversion of free methane gas to hydrates results in uncertainty as to resistivity change.

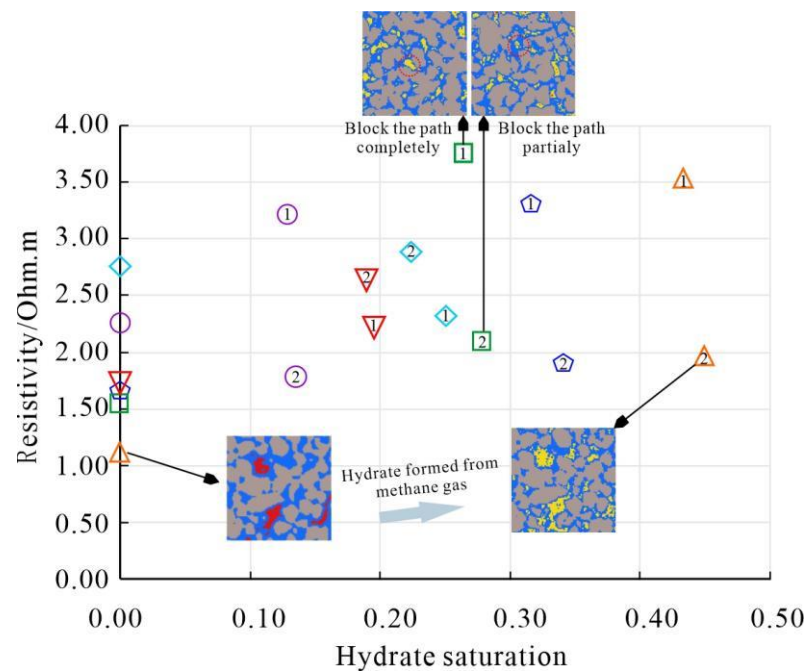


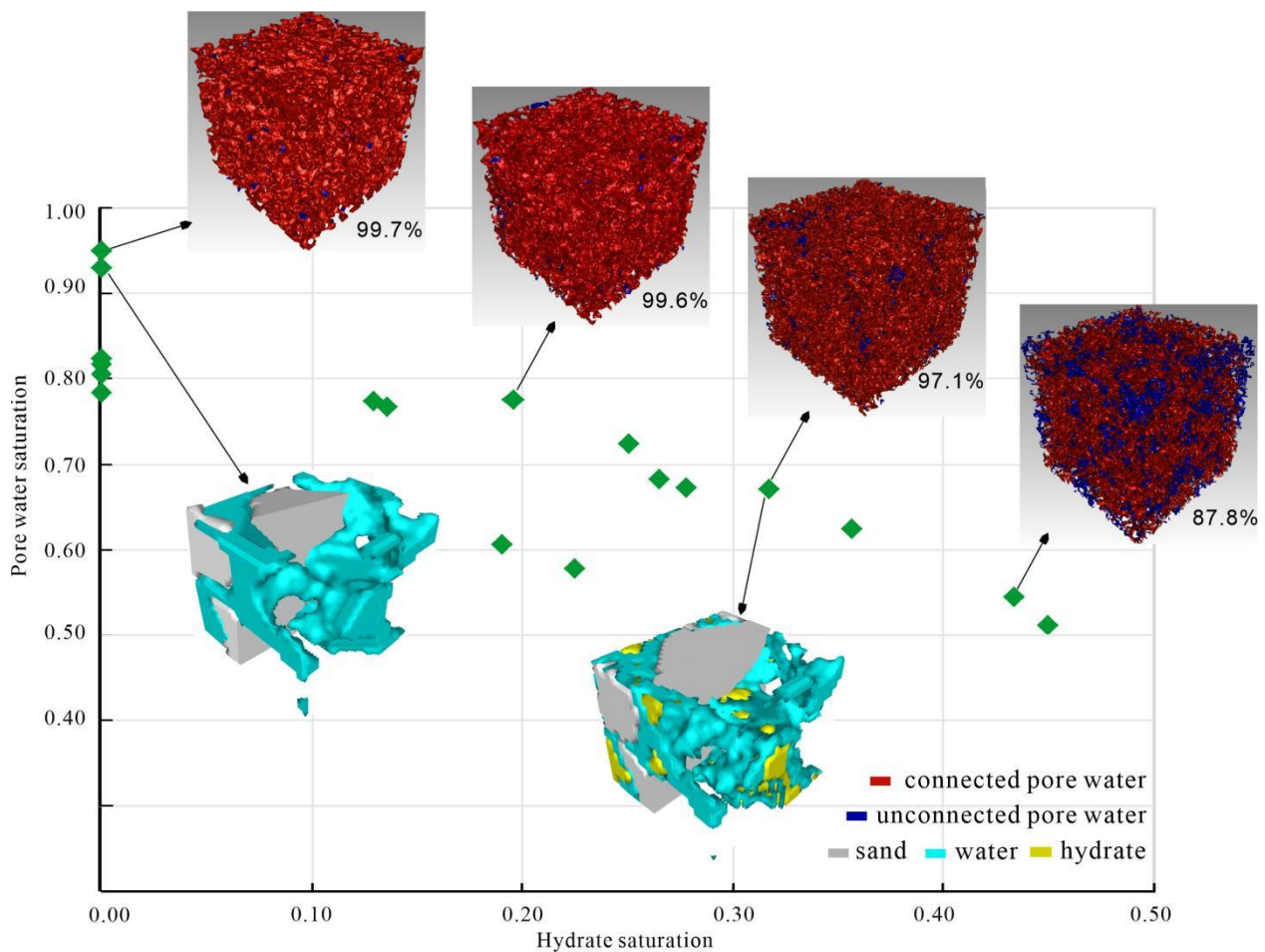
**Figure 3.** The resistivity of hydrate-bearing sediments under different hydrate saturations. Different symbol shapes represent, respectively, the six tests described in Table 1: triangles represent test 1, pentagons represent test 2, squares represent test 3, circles represent test 4, inverted triangles represent test 5, and rhombuses represent test 6. Numbers 1 and 2 located at the middle of symbols represent the upper and lower layers, respectively. Six representative data located at the left x-axis are from the initial state in which hydrate saturation is zero.

### 3.2. The Effect of Hydrates on Pore Water Characteristics

Pore water, as the main conductive medium, is analyzed to reveal the relationship between resistivity and pore water saturation in hydrate-bearing sediments. Pore water of hydrate-bearing sediments is extracted from the three-dimensional X-CT images. According

to the topological connection relationship between pore water and other components in the X-CT image, quantitative information about pore water is provided, including pore water number, maximum pore water volume, tortuosity, and average coordination number. Tortuosity is defined as the ratio of the length of the path to the distance between its ends along the z-axis, which depicts the complexity of the path. Coordination number is defined as the number of throats connected with a pore body, which describes the interconnection among pores. The average coordination number is used in this study because the pore water number is variable.

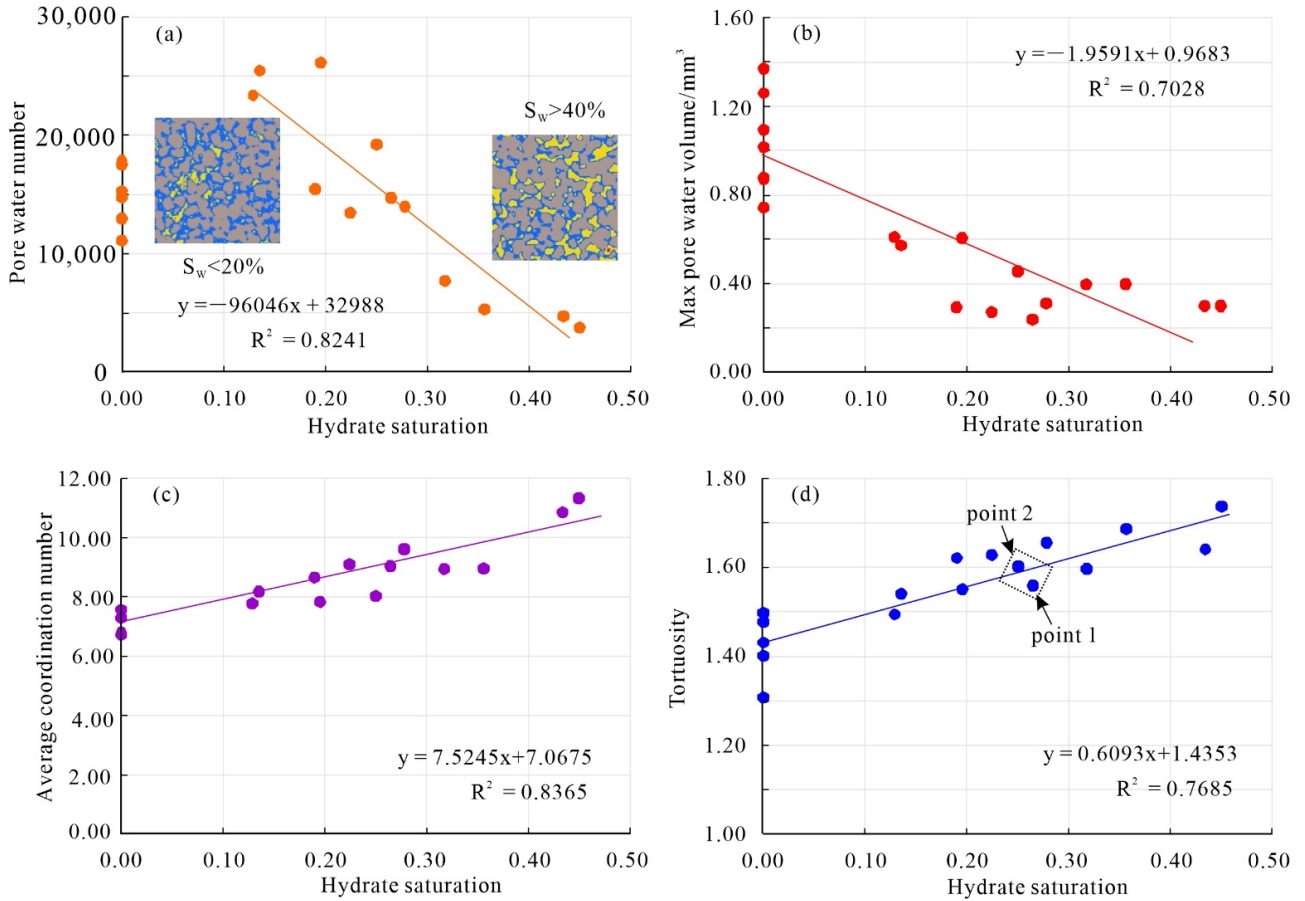
Results show that pore water gradually decreases with the increase of hydrate saturation (Figure 4). The pore water distribution changes obviously from the three-dimensional X-CT images below in Figure 3. The initial pore water is replaced by hydrates in some places and pore water in a pore is divided into several parts. Connected pore water also decreases gradually in the three-dimensional X-CT images presented above in Figure 3. In other words, the isolation effect of hydrates on pore water becomes stronger with the increase of hydrate saturation.



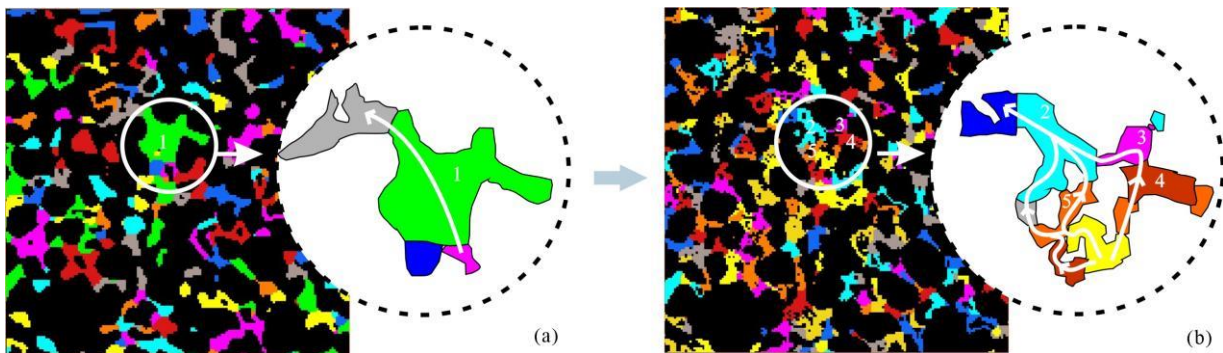
**Figure 4.** The content and distribution changes of pore water versus hydrate saturation. Six representative data of the initial state (hydrate saturation is zero) are presented. The three-dimensional X-CT images above show the pore water extracted from the three-dimensional X-CT images of the hydrate-bearing sediments. The three-dimensional X-CT images below show the distribution of pore water in a pore before (left) and after hydrate formation (right).

Figure 5 depicts the geometrical factors of pore water under different hydrate saturations, including pore water number, maximum pore water volume, average coordination number and tortuosity. The linear relationship between the geometrical factors of pore water and hydrate saturation is observed. Pore water number increases first and then

decreases gradually as hydrate saturation increases (Figure 5a). Maximum pore water volume decreases gradually (Figure 5b). When hydrate saturation is less than 0.2, most hydrates are distributed in the middle of the pore (Figure 5a). Large pore water is divided into several tiny pores, resulting in an increase in pore water number (Figure 6). However, when hydrate saturation is more than 0.4, the hydrate completely displaces the pore water, leading to the increase of pore water number (Figure 5a).



**Figure 5.** The geometrical factors of pore water versus hydrate saturation, and the linear relationship between hydrate saturation and geometrical factors of pore water, including pore water number in (a), maximum pore water volume in (b), average coordination number in (c) and tortuosity in (d).  $R^2$  is the correlation coefficient of the linear relationship.



**Figure 6.** Comparison of pore water number before (a) and after (b) the formation of hydrates in two-dimensional X-CT images. Pore water is separated into lots of pores according to the topological connection relationship between pore water molecules. A pore is divided into five pores which leads to a greater coordination number and more tortuous paths of pore water.

Theoretically, the greater the average coordination number of pore water is, the better the connectivity of pore water. Average coordination number increases with hydrate saturation, which indicates that the connectivity of pore water gradually becomes stronger (Figure 5c). However, the connectivity of pore water is reduced due to the existence of hydrates [8]. The reduction of connected pore water saturation is also observed in Figure 3. As mentioned earlier in this study, large pore water is divided into several tiny pores, which leads to a greater number of small throats. As a result, the average coordination number increase cannot be used to describe the connectivity of pore water in hydrate-bearing sediments.

Hydrate formation will lead to different enhancement degrees of tortuosity [24]. In this study, hydrates make the tortuosity of pore water increase, while the changes (<0.4) are not obvious (Figure 5d). This means that the distribution of pore water becomes a little complicated. In the quadrilateral area of Figure 5d, there is a discrepancy in tortuosity when the hydrate saturation is similar. Pore water number is related to the distribution of pore water. The pore water number of point 1 is less than point 2. That means the distribution of pore water in point 2 is more complicated than that in point 1. Therefore, the tortuosity fluctuates a little with the increase of hydrate saturation. The resistivity of the rock is controlled by the tortuosity of the paths for current flow [34,35]. Compared with the initial large path, current will pass through a more tortuous and narrower path (Figure 6). Consequently, the resistivity of hydrate-bearing sediments increases.

### 3.3. The Effect of Pore Water Characteristics on the Saturation Exponent

According to Archie’s law [10], the relationship between the resistivity and water saturation of hydrate-bearing sediments can be expressed as:

$$I = \frac{R_t}{R_0} = \frac{1}{S_w^n} \tag{1}$$

where I is defined as the resistivity index, dimensionless number;  $R_t$  is the resistivity of hydrate-bearing sediments,  $\Omega \cdot m$ ;  $R_0$  is the resistivity of water-saturated sediments,  $\Omega \cdot m$ ;  $S_w$  is the water saturation, fraction; n is the saturation exponent, dimensionless number.

Then, n can be written as:

$$n = \log_{S_w} \left( \frac{R_0}{R_t} \right) \tag{2}$$

We can get the values of the saturation exponent (n) of hydrate-bearing sediments with different hydrate saturations. The maximum saturation exponent of porous rock recorded in the literature is 6 [34]. Respecting gas hydrates, previous studies have shown that the value range of n is between 1 and 6.65 [5,22,23,36]. In this study, saturation exponents vary from 1.58 to 6.84, almost distributed in the range of less than 6 (Figure 7). This result illustrates that the saturation exponent is a variable value rather than a constant.

In Section 3.2 of this study, the average coordination number fails to represent pore water connectivity. Therefore, we extracted connected pore water from three-dimensional X-CT images and calculated the porosity and saturation of the connected pore water. The expressions are written as:

$$\varphi_c = \frac{V_c}{V} \tag{3}$$

$$S_c = \frac{V_c}{V_\varphi} \tag{4}$$

where  $\varphi_c$  is defined as the porosity of the connected pore water, fraction;  $V_c$  is the volume of the connected pore water; V is the whole volume of sediment;  $S_c$  is the connected pore water saturation, fraction;  $V_\varphi$  is the volume of pores in sediments.

We observe that the saturation exponent increase linearly with the increase of the porosity and saturation of the connected pore water (Figure 8). This indicates that the saturation exponent is dependent on the connectivity of pore water. Tao et al. proposed that the saturation exponents of porous rocks are a function of pore water saturation and

porosity [37]. Dong et al. concluded that the relationship between the saturation exponent and pore water saturation in hydrate-bearing sediments could be expressed in a logarithmic form [23]. The increase of the saturation exponent with pore water saturation was also observed in this study (Figure 9).

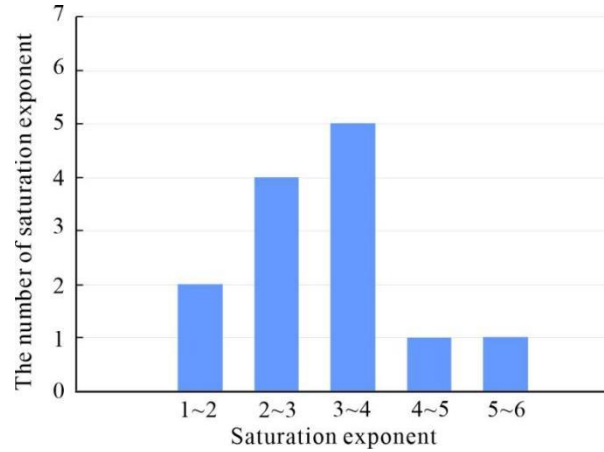


**Figure 7.** The distribution of the saturation exponent (n). The x-axis indicates the range of saturation exponent values. The y-axis represents the number of saturation exponents in a certain range of saturation exponent values.

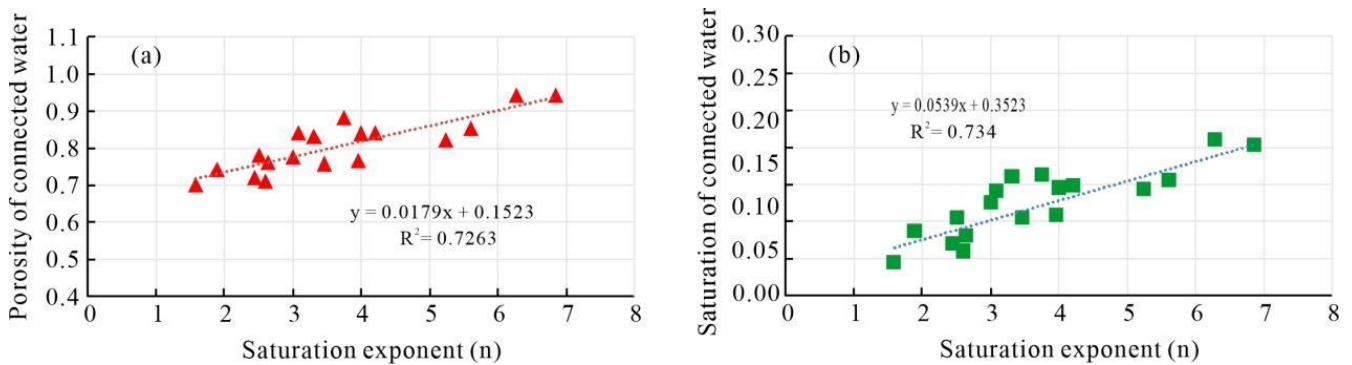


**Figure 8.** The saturation exponent versus connected water characteristics and the linear relationship between the saturation exponent and connected water characteristics, including the porosity in (a) and saturation of connected water in (b).  $R^2$  is the correlation coefficient of the linear relationship.

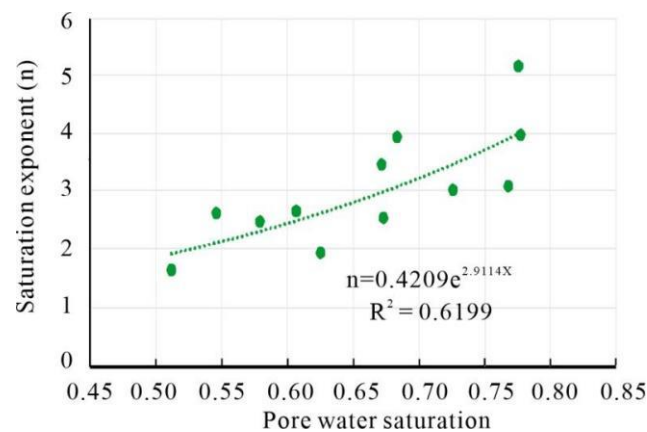


**Figure 9.** The saturation exponent versus pore water saturation.

It is evident that the saturation exponent changes a little at stages of high hydrate saturation and changes significantly at low hydrate saturation stages. This phenomenon is discovered in Chen's result [38]. As hydrates distribute in the middle of pores and pore water number increases, more complicated pore structures and pore water distributions are generated at low hydrate saturation stages. When hydrate saturation is greater than 0.3, the hydrates occupy almost the whole pore. Meanwhile, the pore water number is less than the initial pore water number. The change of pore structure will become slower with the increase of hydrate saturation. Therefore, the distribution of pore water may be the reason why the saturation exponent changes significantly at low hydrate saturation levels and changes a little at high hydrate saturation stages. Previous research also suggests that the saturation exponent is significantly dependent on the distribution of fluids in the pore space [39,40]. It is a challenge to acquire hydrates with high saturation in a physical simulation experiment, which makes it impossible to analyze the evolution of the saturation exponent with pore water saturation from 0 to 100% on this basis.

Tortuosity is a geometric parameter related to electrical properties [16]. Zhang et al. concluded that the tortuosity evolution behavior of effective pores controls the saturation exponent of hydrate-bearing sediments [24]. There is a logarithmic relationship between the saturation exponent and tortuosity of pore water in hydrate-bearing sediments (Figure 10a). The pore water saturation calculated by an experimental fitting model is consistent with pore water saturation from three-dimensional X-CT images (Figure 10b).

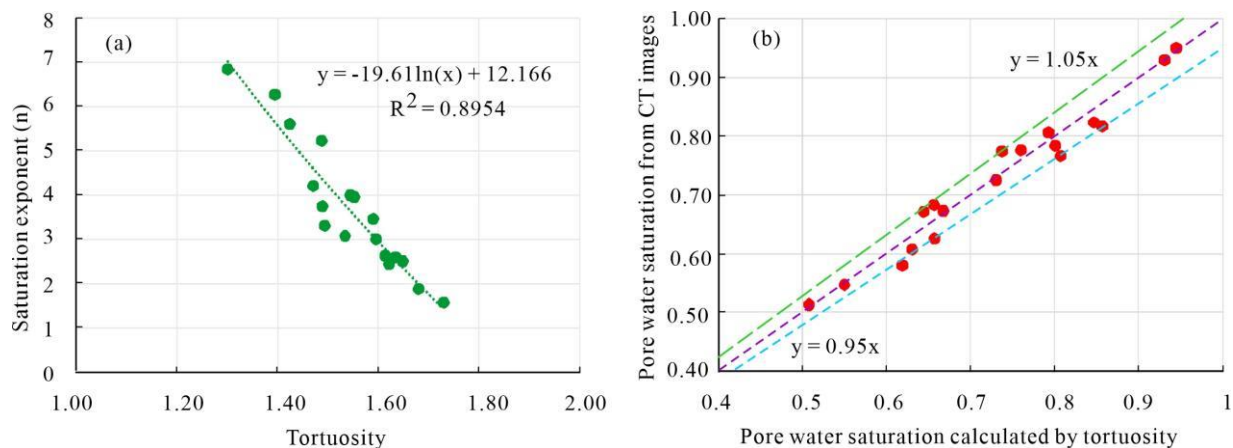


**Figure 10.** The experimental fitting mode of the saturation exponent and tortuosity in this study (a) and the comparison between the pore water saturation calculated by the experimental fitting model and from X-CT images (b). The relative errors are almost less than 5%.

Figure 11 shows the comparison of the experimental data generated in this study or the experimental data of previous research and two marine, coarse-grained reservoirs (Figure 11). The experimental data in this study generally fall within a range of 2–5 of the saturation exponent, which is higher than that of previous experimental results. However, it matches well with the logging data from Gulf of Mexico Holes WR313-H and GC955-H, especially at the low water saturation. Therefore, the fitting model in this study is a suitable method to derive the saturation exponent for calculating field hydrate saturation using resistivity logging data. The pore habits of hydrates are diverse, which leads to complicated pore water characteristics. Meanwhile, the influence of capillary effects and grain size on the relationship between the resistivity index and saturation exponent becomes manifest when water saturation is below 40% [5]. More physical simulation experiments are needed to acquire high hydrate saturation and investigate the effect of pore water characteristics on the saturation exponent.

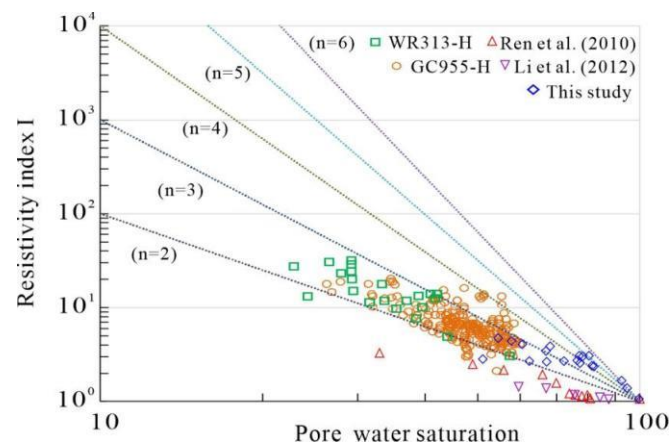


**Figure 11.** Comparison of the resistivity index from the fitting model and the results of previous research [17].

#### 4. Conclusions

The joint measurement of X-ray computed tomography and resistivity provides a feasible approach to characterize the electrical properties and investigate the saturation exponent of Archie's law of hydrate-bearing sediments at the micro-scale. Pore water characteristics and their effect on saturation exponents are analyzed in this study. The main conclusions are as follows:

The resistivity of hydrate-bearing sediments varies with the change of pore water characteristics caused by hydrate formation. Pore water distribution and the proportion of connected pore water changes with hydrate saturation. With the increase of hydrate saturation, initial large pore water is divided into several small pores, result in a greater number of small and tortuous throats. Both the tortuosity and average coordination number gradually increase. Compared with the initial large path, current will pass through a smaller and narrower path, which leads to an increase in the resistivity of hydrate-bearing sediments.

The saturation exponent of Archie's law is controlled by the distribution and connectivity of pore water. The saturation exponent increases with the porosity and saturation of connected pore water. Complicated pore structures at low hydrate saturation levels result in a significant change in saturation exponents. There is a logarithmic relationship between the saturation exponent and the tortuosity of pore water. The saturation exponent calculated by tortuosity of pore water is consistent with the results based on the logging data.

**Author Contributions:** Research design, J.Z.; experiments, J.Z., Q.B. and Y.L.; data analysis, J.Z., C.L. (Chengfeng Li) and Y.Z.; writing—original draft preparation, J.Z.; supervision, Q.C.; writing—review and editing, C.L. (Changling Liu) and N.W. All authors have read and agreed to the published version of the manuscript.

**Funding:** This research was funded by the National Natural Science Foundation of China (No. 41906067) and the Shandong Provincial Natural Science Foundation (No. ZR2019BD051).

**Institutional Review Board Statement:** Not applicable.

**Informed Consent Statement:** Not applicable.

**Data Availability Statement:** The data that support the findings of this paper are available within the article.

**Conflicts of Interest:** The authors declare no conflict of interest.

## References

1. Boswell, R.; Hancock, S.; Yamamoto, K.; Collett, T.; Pratap, M.; Lee, S. Natural gas hydrates: Status of potential as an energy resource. In *Future Energy*; Elsevier: Amsterdam, The Netherlands, 2020; pp. 111–131.
2. Pearson, C.; Murphy, J.; Hermes, R. Acoustic and resistivity measurements on rock samples containing tetrahydrofuran hydrates: Laboratory analogues to natural gas hydrate deposits. *J. Geophys. Res. Solid Earth* **1986**, *91*, 14132–14138. [[CrossRef](#)]
3. Shankar, U.; Riedel, M. Assessment of gas hydrate saturation in marine sediments from resistivity and compressional-wave velocity log measurements in the Mahanadi Basin, India. *Mar. Pet. Geol.* **2014**, *58*, 265–277. [[CrossRef](#)]
4. Sun, Y.; Goldberg, D.; Collett, T.; Hunter, R. High-resolution well-log derived dielectric properties of gas-hydrate-bearing sediments, Mount Elbert gas hydrate stratigraphic test well, Alaska north slope. *Mar. Pet. Geol.* **2011**, *28*, 450–459. [[CrossRef](#)]
5. Spangenberg, E.; Kulenkampff, J. Influence of methane hydrate content on electrical sediment properties. *Geophys. Res. Lett.* **2006**, *33*, 315–319. [[CrossRef](#)]
6. Lee, J.Y.; Santamarina, J.C.; Ruppel, C. Parametric study of the physical properties of hydrate-bearing sand, silt, and clay sediments: 1. Electromagnetic properties. *J. Geophys. Res.* **2010**, *115*, B11104. [[CrossRef](#)]
7. Jia, J.H.; Tsuji, T.; Matsuoka, T. Gas hydrate saturation and distribution in the Kumano Forearc Basin of the Nankai Trough. *Explor. Geophys.* **2016**, *48*, 137–150. [[CrossRef](#)]
8. Ren, A.R.; Liu, Y.J.; Liu, Y.X.; Zhang, W.D. Acoustic velocity and electrical resistance of hydrate bearing sediments. *J. Pet. Sci. Eng.* **2010**, *70*, 52–56. [[CrossRef](#)]
9. Jin, Y.R.; Li, S.X.; Yang, D.Y. Experimental and theoretical quantification of the relationship between electrical resistivity and hydrate saturation in porous media. *Fuel* **2020**, *269*, 117378. [[CrossRef](#)]
10. Archie, G.E. The electrical resistivity log as an aid in determining some reservoir characteristics. *Trans. Am. Inst. Min. Metall. Eng.* **1942**, *146*, 54–61. [[CrossRef](#)]
11. KÜntz, M.; Mareschal, J.C.; Lavallée, P. Numerical estimation of electrical conductivity in saturated porous media with a 2-D lattice gas. *Geophysics* **2000**, *65*, 766–772. [[CrossRef](#)]
12. Kennedy, W.; Herrick, D. Conductivity models for Archie rocks. *Geophysics* **2012**, *77*, WA109–WA128. [[CrossRef](#)]
13. Yue, W.Z.; Dong, G. A new non-Archie model for pore structure: Numerical experiments using digital rock models. *Geophys. J. Int.* **2013**, *195*, 282–291. [[CrossRef](#)]
14. Choo, H.; Burns, S.E. Review of Archie's equation through theoretical derivation and experimental study on uncoated and hematite coated soils. *J. Appl. Geophys.* **2014**, *105*, 225–234. [[CrossRef](#)]
15. Ghanbarian, B.; Hunt, A.G.; Ewing, R.P.; Skinner, T.E. Universal scaling of the formation factor in porous media derived by combining percolation and effective medium theories. *Geophys. Res. Lett.* **2014**, *41*, 3884–3890. [[CrossRef](#)]
16. Cai, J.C.; Wei, W.; Hu, X.Y.; Wood, D.A. Electrical conductivity models in saturated porous media: A review. *Earth-Sci. Rev.* **2017**, *171*, 419–433. [[CrossRef](#)]
17. Cook, A.E.; Waite, W.F. Archie's saturation exponent for natural gas hydrate in Coarse-Grained Reservoirs. *J. Geophys. Res. Solid Earth* **2018**, *123*, 2069–2089. [[CrossRef](#)]
18. Yue, W.Z. Pore-Scale explanation of the Archie's cementation exponent: Microstructure, electrical anisotropy, and numerical experiments. *Geophys. Res. Lett.* **2019**, *46*, 5799–5807. [[CrossRef](#)]
19. Wang, X.J.; Lee, M.; Collet, T.; Yang, S.X.; Guo, Y.Q.; Wu, S.G. Gas hydrate identified in sand-rich inferred sedimentary section using downhole logging and seismic data in Shenhu area, South China Sea. *Mar. Pet. Geol.* **2014**, *51*, 298–306. [[CrossRef](#)]
20. Kim, H.S.; Cho, G.C.; Lee, J.Y.; Kim, S.J. Geotechnical and geophysical properties of deep marine fine-grained sediments recovered during the second Jlleung Basin Gas Hydrate expedition, East Sea, Korea. *Mar. Pet. Geol.* **2013**, *47*, 56–65. [[CrossRef](#)]
21. Santamarina, J.C.; Ruppel, C. The impact of hydrate saturation on the mechanical, electrical, and thermal properties of hydrate-bearing sand, silts, and clay. In Proceedings of the 6th International Conference on Gas Hydrates, Vancouver, BC, Canada, 6–10 July 2008.
22. Pandey, L.; Sain, K.; Joshi, A.K. Estimate of gas hydrate saturations in the Krishna-Godavari basin, eastern continental margin of India, results of expedition NGHP-02. *Mar. Pet. Geol.* **2019**, *108*, 581–594. [[CrossRef](#)]
23. Dong, H.M.; Sun, J.M.; Zhu, J.J.; Liu, L.; Lin, Z.Z.; Golsanami, N.; Cui, L.K.; Yan, W.C. Developing a new hydrate saturation calculation model for hydrate-bearing sediments. *Fuel* **2019**, *248*, 27–37. [[CrossRef](#)]
24. Zhang, Z.; Liu, L.L.; Li, C.F.; Cai, J.C.; Nin, F.L.; Meng, Q.G.; Liu, C.L. Fractal analyses on saturation exponent in Archie's law for electrical properties of hydrate-bearing porous media. *J. Pet. Sci. Eng.* **2021**, *196*, 107642. [[CrossRef](#)]
25. Seol, Y.; Kneafsey, T.J. X-ray computed-tomography observations of water flow through anisotropic methane hydrate-bearing sand. *J. Pet. Sci. Eng.* **2009**, *66*, 121–132. [[CrossRef](#)]
26. Sell, K.; Quintal, B.; Kersten, M.; Saenger, E.H. Squirt flow due to interfacial water films in hydrate bearing sediments. *Solid Earth* **2018**, *9*, 699–711. [[CrossRef](#)]
27. Han, G.; Kwon, T.H.; Lee, J.Y.; Kneafsey, T.J. Depressurization-induced fines migration in sediments containing methane hydrate X-ray computed tomography imaging experiments. *J. Geophys. Res. Solid Earth* **2018**, *123*, 2539–2558. [[CrossRef](#)]
28. Lei, L.; Liu, Z.C.; Seol, Y.; Boswell, R.; Dai, S. An investigation of hydrate formation in unsaturated sediments using X-ray computed tomography. *J. Geophys. Res. Solid Earth* **2019**, *124*, 3335–3349. [[CrossRef](#)]
29. Lei, L.; Seol, Y.; Choi, J.H.; Kneafsey, T.J. Pore habit of methane hydrate and its evolution in sediment matrix-laboratory visualization with phase-contrast micro-CT. *Mar. Pet. Geol.* **2019**, *104*, 451–467. [[CrossRef](#)]

30. Li, C.F.; Liu, C.L.; Hu, G.W.; Sun, J.Y.; Hao, X.L.; Liu, L.L.; Meng, Q.G. Investigation on the multiparameter of hydrate-bearing sands using nano-focus X-ray computed tomography. *J. Geophys. Res. Solid Earth* **2019**, *124*, 2286–2296. [[CrossRef](#)]
31. You, K.; Flemings, P.B.; Malinverno, A.; Collett, T.S.; Darnell, K. Mechanisms of methane hydrate formation in geological systems. *Rev. Geophys.* **2019**, *57*, 1146–1196. [[CrossRef](#)]
32. Patmonoaji, A.; Hu, Y.; Nasir, M.; Zhang, C.; Suekane, T. Effects of dissolution fingering on mass transfer rate in three-dimensional porous media. *Water Resour. Res.* **2021**, *57*, e2020WR029353. [[CrossRef](#)]
33. Sahoo, S.K.; Madhusudhan, B.N.; Marín-Moreno, H.; North, L.J.; Ahmed, S.; Falcon-Suarez, I.H.; Minshull, T.A.; Best, A.I. Laboratory insights into the effect of sediment-hosted methane hydrate morphology on elastic wave velocity from time-lapse 4-D synchrotron X-ray computed tomography. *Geochem. Geophys. Geosyst.* **2018**, *19*, 4502–4521. [[CrossRef](#)]
34. Sharma, M.M.; Garrouch, A.; Dunlap, H.F. Effects of wettability, pore geometry, and stress on electrical conduction in fluid-saturated rocks. *Log Anal.* **1991**, *32*, 511–526.
35. Xing, L.C.; Qi, S.Y.; Xu, Y.; Wang, B.; Lao, L.Y.; Wei, W.; Han, W.F.; Wei, Z.T.; Ge, X.M.; Aliyu, A.M. Numerical study on complex conductivity characteristics of hydrate-bearing porous media. *J. Nat. Gas Sci. Eng.* **2021**, *95*, 104145. [[CrossRef](#)]
36. Wu, P.; Li, Y.h.; Sun, X.; Liu, W.G.; Song, Y.C. Pore-scale 3D morphological modeling and physical characterization of hydrate-bearing sediment based on computed tomography. *J. Geophys. Res. Solid Earth* **2020**, *125*, e2020JB020570. [[CrossRef](#)]
37. Tao, G.; Yue, W.Z.; Li, B.T.; Fang, C.L. Electrical transport properties of fluid-saturated porous rocks by 2D lattice gas automata. *SPE Reserv. Eval. Eng.* **2006**, *9*, 274–279. [[CrossRef](#)]
38. Chen, Y.F.; Li, D.L.; Liang, D.Q.; Zhou, X.B.; Wu, N.Y. Relationship between gas hydrate saturation and resistivity in sediments of the South China Sea. *Acta Pet. Sin.* **2013**, *34*, 507–512.
39. Man, H.N.; Jing, X.D. Network modelling of wettability and pore geometry effects on electrical resistivity and capillary pressure. *J. Pet. Sci. Eng.* **1999**, *24*, 255–267. [[CrossRef](#)]
40. Spangenberg, U. Modeling of the influence of gas hydrate content on the electrical properties of porous sediments. *J. Geophys. Res.* **2001**, *106*, 6535–6548. [[CrossRef](#)]